EJNMMI Physics

ORIGINAL RESEARCH

Open Access

Feasibility of simplified Patlak parametric imaging with scaled population-based input function on pancreatic cancer

Zhixin Hao[1†], Haiqiong Zhang[1†], Yonghong Dang[1], Jiangdong Qiu[2], Mengshi Yan[3], Xinchun Yan[1], Zhenghai Huang[4], Chao Ren[1], Taiping Zhang[2*], Wenming Wu[2*] and Li Huo[1*]

†Zhixin Hao and Haiqiong Zhang contributed equally to this work.

*Correspondence:
Taiping Zhang
tpingzhang@yahoo.com
Wenming Wu
doctorwuu@126.com
Li Huo
huoli@pumch.cn
[1]Department of Nuclear Medicine, State Key Laboratory of Complex Severe and Rare Diseases, Center for Rare Diseases Research, Beijing Key Laboratory of Molecular Targeted Diagnosis and Therapy in Nuclear Medicine, Peking Union Medical College Hospital, Chinese Academy of Medical Science and Peking Union Medical College, Beijing 100730, China
[2]Department of General Surgery, Peking Union Medical College Hospital, Chinese Academy of Medical Science and Peking Union Medical College, Beijing 100730, China
[3]Beijing United Imaging Research Institute of Intelligent Imaging, Beijing 100094, China
[4]Medical Science Research Center, Peking Union Medical College Hospital, Chinese Academy of Medical Science and Peking Union Medical College, Beijing 100730, China

Abstract

Background This study evaluates the feasibility of using a simplified Patlak parametric imaging technique with a scaled population-based input function (sPBIF) in pancreatic cancer.

Methods Twenty-six patients underwent multi-bed, multi-pass [^{18}F]FDG PET/CT scans, from which both dynamic and static PET images were reconstructed. Patlak parametric images were generated from the dynamic PET series using both the image-derived input function (IDIF) and the sPBIF. The consistency between IDIF and sPBIF was evaluated by comparing the area under the curve (AUC) and Patlak parameters derived from both input functions. The detectability of pancreatic lesions, assessed by tumor-to-background ratio (TBR) and contrast-to-noise ratio (CNR), was compared between SUV and Patlak parametric images. Additionally, the correlation between clinicopathological features and PET parameters, including SUV and Patlak values, was analyzed.

Results We found good agreement between the AUC for IDIF and sPBIF with correlation coefficients of 0.87 and 0.93 for the 0–30 min and 0–50 min intervals, respectively. The Patlak parameters from IDIF and sPBIF presented correlation coefficients higher than 0.94. The SUV and Patlak K_i exhibited correlation coefficients greater than 0.92 and 0.73 in malignant and benign pancreatic lesions, respectively. The SUV and Patlak V_0 correlated with correlation coefficients higher than 0.75 in benign lesions, but exhibited only a weak correlation in malignant lesions. The TBR of Patlak K_i was significantly higher in malignant lesions compared to SUV. However, the CNR of Patlak K_i was lower due to increased noise in the parametric images. Most clinicopathological features showed weak correlation with PET parameters, except for a marginal classification of lesion differentiation by the maximum K_i value.

Conclusions The sPBIF approach enables the acquisition of additional Patlak parametric images alongside static SUV imaging in pancreatic cancer patients. K_i parametric imaging provided higher contrast than static imaging for detecting pancreatic lesions.

Keywords [^{18}F]FDG, Patlak parametric imaging, Scaled PBIF, Pancreatic cancer

Introduction

Pancreatic ductal adenocarcinoma (PDAC) is projected to become the second leading cause of cancer-related deaths in the United States by 2030. Complete surgical resection remains the only curative treatment; however, only 20% of patients present with potentially resectable disease. Among those who undergo surgery, the survival rate is approximately 23% [1]. Imaging plays a critical role in the detection, staging, and surgical planning of pancreatic tumors. Contrast-enhanced CT (CE-CT) is the most used modality for evaluating pancreatic malignancies, but its ability to detect small primary and metastatic lesions is limited [2].

Positron emission tomography (PET) offers a significant advantage in diagnosing and monitoring pancreatic cancer, as it measures the physiological and pathological functions of tissues through the spatial and temporal distribution of radioactive tracers [3–6]. [^{18}F]-fluorodeoxyglucose (FDG) is a widely used PET tracer in clinical practice, and [^{18}F]FDG PET/CT has been extensively applied in the diagnosis and management of pancreatic cancer [7–10]. The sensitivity of [^{18}F]FDG PET/CT for diagnosing pancreatic cancer ranges from 90 to 95%, with specificity between 82% and 100% [11]. Despite its essential role, [^{18}F]FDG PET/CT has limitations, particularly when semi-quantitative uptake measurements are affected by factors such as the uptake period after injection, lesion size, blood glucose levels, and insulin levels [12].

Pharmacokinetic analysis offers a solution by breaking down tracer uptake into independent parameters that reflect the physiological or pathological properties of the tissue. However, despite the potential benefits, parametric imaging has not been widely adopted in clinical practice, primarily due to challenges in accurately determining the arterial input function (AIF), which is crucial for pharmacokinetic modeling [13–16]. The gold standard for the input function determination is arterial blood sampling throughout the dynamic PET scan, but its invasiveness limits widespread use. Non-invasive alternatives like the image-derived input function (IDIF) [17] are attractive but come with challenges such as partial volume correction and interference from radioactive metabolites [18–22]. Another alternative is the population-based input function (PBIF), which uses a modeled average input function across a population [23–25]. The PBIF resembles the input function of a test individual on condition that it is derived from a representative population. The PBIF can be individualized into the scaled population-based input function (sPBIF) by scaling according to individual's input function [26, 27]. PBIF and sPBIF simplify pharmacokinetic modeling by providing input function data before the scan.

The Patlak graphical method is commonly used in parametric imaging, offering values for the net influx rate (K_i) and apparent distribution volume (V_0) [13, 14]. The utility of Patlak parametric imaging with [^{18}F]FDG PET in oncology has been well-documented [4, 28–30]. However, traditional studies often require extended dynamic PET scans immediately following injection, which are time-consuming. Recent advancements suggest that shortened dynamic PET scans integrated with PBIF can simplify Patlak parametric imaging, allowing the generation of additional parametric images without disrupting clinical workflows [26, 27, 31, 32].

Although prior research [26, 27, 31, 32] has explored the potential of PBIF-based simplified Patlak parametric imaging, the consistency between IDIF- and PBIF-based Patlak imaging has not been specifically examined in pancreatic cancer. This study investigates the feasibility of simplified Patlak imaging with sPBIF in pancreatic cancer. We assess the

consistency between sPBIF and IDIF Patlak analyses, evaluate the diagnostic potential of Patlak parameters in lesion detection, and explore their relationship with clinicopathological features.

Materials and methods

Patient population

Twenty-six patients with suspected pancreatic cancer, as identified by CE-CT, were consecutively enrolled in this study. None of the patients had received any treatment before the examinations. This prospective study was approved by the Institutional Review Board of Peking Union Medical University Hospital (Approval No. K4068), and all participants provided informed consent before undergoing the dynamic [^{18}F]FDG PET/CT scan. Detailed patient characteristics are provided in Table 1. Of the participants, twenty were diagnosed with pancreatic ductal adenocarcinoma, while the remaining six were diagnosed with other conditions: one with intraductal papillary mucinous neoplasm, two with mucinous cystic neoplasm, two with serous cystic neoplasm, and one with mass-forming chronic pancreatitis.

All suspected lesions were confirmed through surgery or biopsy. Serum carbohydrate antigen 19 – 9 (CA 19 – 9) levels were recorded prior to the PET/CT scan. For patients who underwent surgery and were diagnosed with pancreatic cancer, tumor size, grade of differentiation, vascular invasion, perineural invasion, and lymph node metastasis were

Table 1 Patient characteristics

Characteristics	Data
All patients (*n* = 26)	
Age	62 ± 8
Sex	
Male	12 (46.2%)
Female	14 (53.8%)
Treatment	
Surgery	18 (69.2%)
Biopsy	8 (30.8%)
Pathology	
Pancreatic ductal adenocarcinoma	20 (77.0%)
Intraductal papillary mucinous neoplasm	1 (3.8%)
Mucinous cystic neoplasm	2 (7.7%)
Serous cystic neoplasm	2 (7.7%)
Mass-forming chronic pancreatitis	1 (3.8%)
Pancreatic cancer patients diagnosed by surgery (*n* = 14)	
Serum CA 19 – 9 (U/ml; median, range)	75.2 (2.0–1867.0)
Tumor size (cm; median, range)	3.3 (1.0–5.0)
Differentiation	
1	6 (42.9%)
2, 3	8 (57.1%)
Vascular invasion	
Positive	3 (21.4%)
Negative	11 (78.6%)
Perineural invasion	
Positive	11 (78.6%)
Negative	3 (21.4%)
Lymph nodes metastasis	
Positive	6 (42.9%)
Negative	8 (57.1%)

documented. The degree of differentiation in pancreatic cancer was classified as well-differentiated (grade 1), moderately differentiated (grade 2), or poorly differentiated (grade 3) according to the 2019 World Health Organization classification system. Fourteen pancreatic cancer patients who were diagnosed through surgery were included in the further analysis of clinicopathological features and PET parameters in this study.

PET/CT imaging protocol and image reconstruction

All patients underwent a multi-pass, multi-bed PET/CT scan using a digital PET/CT scanner (uMI Panorama, United Imaging Healthcare, China) with a 35 cm axial field of view (FOV), operating in list mode [33]. Patients fasted for at least 6 h before the scan, and their blood glucose levels were monitored to ensure they were within the range of 4.5–8.8 mmol/L before the injection of [^{18}F]FDG (5.55 MBq/kg). PET/CT imaging commenced immediately after the injection.

The total PET acquisition time was 50 min, consisting of a 10-minute cardiac bed acquisition, followed by a 40-minute multi-bed, multi-pass session, during which there were ten 4-minute passes, and each pass comprised four 1-minute bed positions. The PET images were reconstructed using the ordered-subset expectation maximization algorithm (OSEM) with the following parameters: 2 iterations, 10 subsets, a 600 mm FOV, a 256 × 256 matrix, a slice thickness of 2.9 mm, and a Gaussian filter with a full width at half maximum (FWHM) of 3 mm. The dynamic image series consists of 130 frames, with the first 120 frames reconstructed from the cardiac bed and the last 10 frames reconstructed from the 10 passes. The static standardized uptake value (SUV) image was reconstructed from the last 5 passes. All PET reconstructions included standard corrections for decay, Compton scattering, random events, dead time, attenuation, normalization, and time-of-flight (TOF) and point-spread function (PSF) techniques.

Patlak parametric imaging and graphical method

The Patlak K_i and intercept V_0 parametric images are obtained with uKinetics software with IDIF and sPBIF. Two input functions will be described in a following subsection. Patlak parametric imaging is performed between 30 min and 50 min after injection [34]. Patlak and his colleagues developed a graphical method to determine the macro pharmacokinetic parameters after tracer concentration in the non-displaceable compartment reaches the steady state [13, 14], which uses an approximated relation between the total concentration $C_T(t)$ at time t and the input function $C_P(t)$ both measured by PET,

$$\left(\frac{C_T}{C_P}\right)(t) = K_i \frac{\int_0^t C_P(\tau)\, d\tau}{C_P(t)} + V_0. \tag{1}$$

The area under curve (AUC) of the input function is the integration of the input function from the injection to time t, $\mathrm{AUC}[C_P](t) = \int_0^t C_P(\tau)\, d\tau$. The net tracer influx rate K_i the slope of Eq. (1), is identified by Patlak and Blasberg [14] as $K_i = K_1 k_3/(k_2 + k_3)$ given the assumption of the irreversible 2-tissue-comparment model, while the intercept V_0 denotes the apparent distribution volume, which approximates the sum of blood volume and distribution volume of reversible compartments.

Input functions

IDIF and sPBIF were both used in Patlak parametric imaging in this research. The IDIF was extracted from a cylindrical volume of interest (VOI) with 4-mm transversal radius in the descending aorta automatically segmented using uKinetics (United Imaging Healthcare, China) [35]. Partial volume correction (PVC), radiometabolite correction, and blood-to-plasma ratio (BPR) correction were not applied to the IDIF. The sPBIF was obtained by scaling the PBIF template in uKinetics using the measured activity at 30 min post-injection. The template was generated from the IDIFs of 34 subjects who underwent dynamic [^{18}F]FDG scans on the uEXPLORER PET/CT system at another site. None of these subjects were included in the current study. The processing steps included peak alignment, normalization, and average, as described in a previous study [25]. Figure 1 exemplifies IDIF, sPBIF, and the original PBIF template in uKinetics for a patient subject.

Detection ability assessment

Lesions were visually identified by physicians, and VOIs were manually delineated along the tumor edges on CT images. Both the mean and maximum values were measured for each lesion on SUV and Patlak parametric images. Additionally, a spherical VOI with a diameter of 30 ± 3 mm was manually drawn in a normal region of the right liver lobe on both SUV and Patlak parametric images. The mean and max values and standard deviation σ within this VOI were recorded. The image quality of the SUV and Patlak parametric images was objectively assessed using the tumor-to-background ratio (TBR) and the contrast-to-noise ratio (CNR), as defined in the following equations:

$$\mathrm{TBR}_m = \frac{m_{\mathrm{lesion}}}{mean_{\mathrm{background}}} - 1, \tag{2}$$

$$\mathrm{CNR}_m = \frac{m_{\mathrm{lesion}} - m_{\mathrm{background}}}{\sigma_{\mathrm{background}}}, \tag{3}$$

where m corresponds to the mean and maximum values in the VOI, and the healthy liver VOI serves as the background.

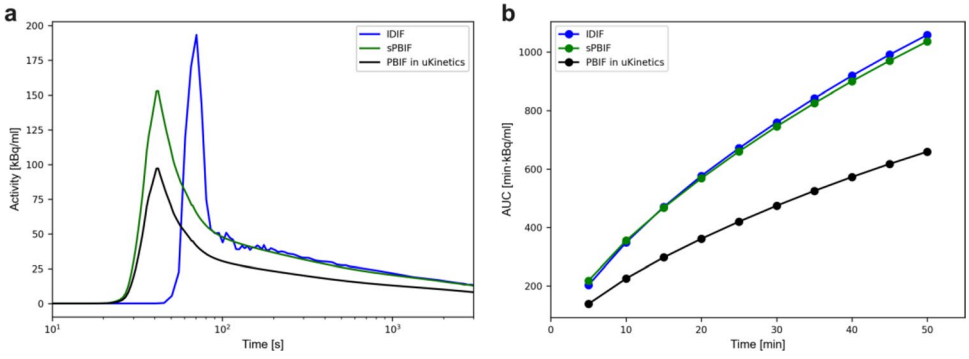

Fig. 1 Comparison among IDIF, PBIF in uKinetics, and sPBIF for a subject. (**a**) The PBIFs and IDIF differ primarily in their peaks. The tails of sPBIF and IDIF overlap after 200 s. The horizontal axis is shown on a logarithmic scale. (**b**) The input functions are compared based on their AUCs in 5-minute intervals. The AUCs of sPBIF and IDIF are close

Statistical analysis

The Shapiro-Wilk test was used to determine whether the quantitative data followed a normal distribution. Data that met this criterion were presented as mean ± σ. The paired *t*-test was employed to compare the statistical differences in TBR and CNR values, with a *P*-value of less than 0.05 considered statistically significant. Pearson correlation analysis was performed to assess the consistency between IDIF and sPBIF, the correlation between SUV and Patlak parameters, and the relationship between PET measurements and various clinicopathological features. Additionally, the mean relative bias was reported to evaluate the consistency between IDIF and sPBIF. All statistical analyses were conducted using the SciPy package (version 1.11.3) [33].

Results

Consistency of Patlak parameters between IDIF and sPBIF

Figure 2 compares the AUC between IDIF and sPBIF for the 0–30 min and 0–50 min intervals. The AUCs of both input functions were highly correlated, with only minor biases observed. Patlak K_i and V_0, derived from both input functions, demonstrated even better consistency, as shown in Fig. 3, for both mean and maximum values within the lesion VOIs. Notably, the biases in the mean K_i and maximum V_0 were negligible.

Uptake of [^{18}F]FDG and Pharmacokinetic analyses

Table 2 summarizes and compares the mean values of SUV and Patlak parameters in malignant and benign pancreatic lesions, as well as in normal liver VOIs. The corresponding maximum value results are provided in Supplemental Table 1. Malignant lesions exhibited higher [^{18}F]FDG uptake than the healthy liver and slightly higher uptake than benign lesions, with SUV and Patlak K_i being highest in malignant lesion VOIs. The apparent distribution volume, Patlak V_0, was similar in malignant and benign lesions but significantly lower in the liver. The net [^{18}F]FDG uptake, as measured by Patlak K_i, was also higher in benign lesions compared to the liver. Patlak parameters derived from IDIF and sPBIF showed minimal differences, as indicated by the σ for the study subjects. SUV and Patlak K_i images of representative cases are shown in Fig. 4.

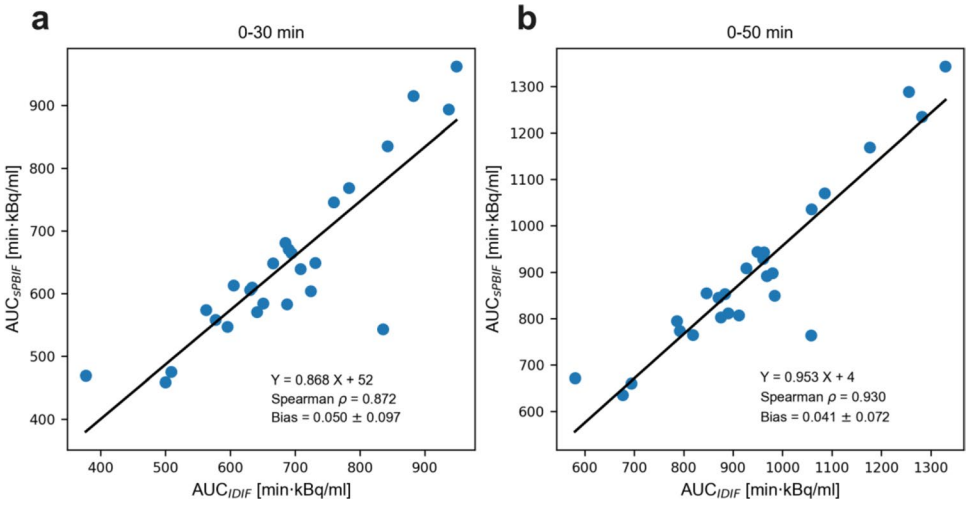

Fig. 2 Correlation of AUC between IDIF and sPBIF for 0–30 min (**a**) and 0–50 min (**b**). The strong correlation of AUCs between IDIF and sPBIF indicates their consistency

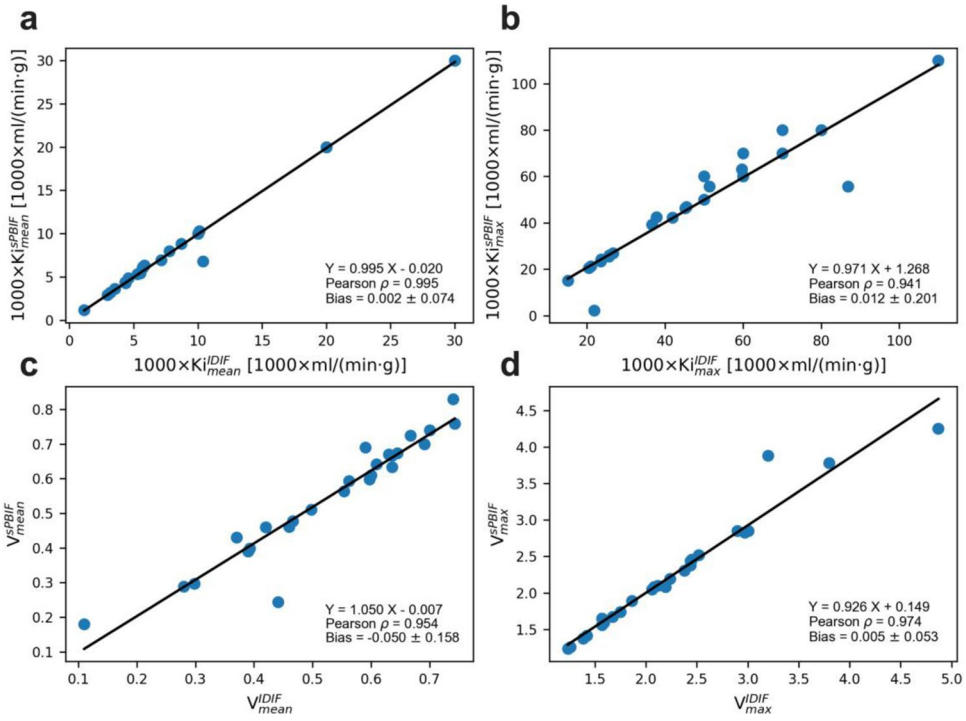

Fig. 3 Correlation of mean and maximum value of Patlak K_i (**a**, **b**) and intercept (V_0; **c**, **d**) of lesion between IDIF and sPBIF. The strong correlation of Patlak parameters between IDIF and sPBIF indicates their consistency

Table 2 The summary of SUV and Patlak parameters in malignant and benign pancreatic lesions and liver

Parameters	SUV	1000* K_i^{IDIF}	1000* K_i^{sPBIF}	V^{IDIF}	V^{sPBIF}
Malignant lesions	$3.83 \pm 1.42^{\#*}$	$11.73 \pm 8.40^{*}$	$11.58 \pm 8.44^{*}$	$0.55 \pm 0.15^{*}$	$0.58 \pm 0.17^{*}$
Benign lesions	$2.05 \pm 0.75^{*}$	$5.64 \pm 2.36^{*}$	$5.75 \pm 2.43^{*}$	$0.47 \pm 0.14^{*}$	$0.48 \pm 0.14^{*}$
Liver	2.66 ± 0.39	3.61 ± 1.62	3.62 ± 1.72	0.93 ± 0.09	0.94 ± 0.08

The values of SUV and Patlak parameters are of mean value in VOIs and reported in terms of mean and σ for included subjects. Note: # for $P < 0.05$ when compared to benign lesion, * for $P < 0.05$ when compared to healthy liver tissue

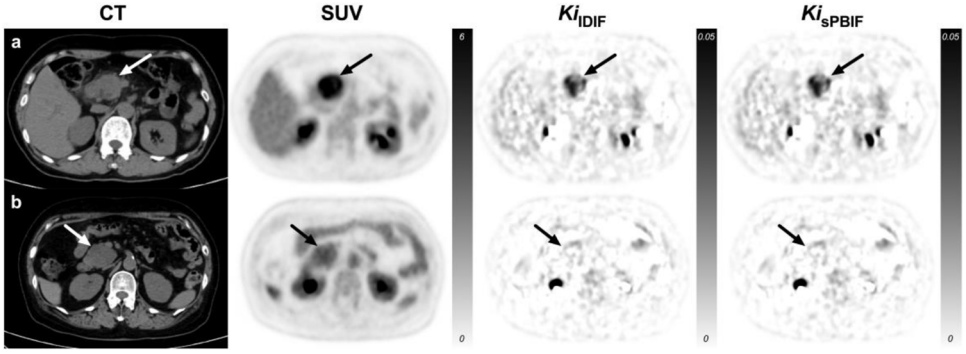

Fig. 4 Examples of malignant and benign pancreatic lesions in CT, SUV images, Ki_{IDIF} images, and Ki_{sPBIF} images. (**a**) Axial images of pancreatic ductal adenocarcinoma in a 59-year-old woman. The images show a mass in the pancreatic head with prominent [^{18}F]FDG uptake, which is clearly visible on Ki images. (**b**) Axial images of serous cystic neoplasm in a 56-year-old woman. The images show a mass in the pancreatic head with mild [^{18}F]FDG uptake. The lesion appears as a "cold spot," with its margins visible on Ki images

Figures 5 and 6 illustrate the correlations between the mean values of SUV and Patlak parameters in lesion VOIs, with corresponding maximum value results provided in Supplemental Figs. 1 and 2. SUV in lesion VOIs was strongly correlated with Patlak K_i, particularly in malignant lesions, where the Pearson correlation coefficient (rho) was 0.926. The correlation between SUV and the Patlak intercept V_0 in malignant lesions is weak, while in benign lesions the SUV positively correlates with Patlak intercept V_0 with the correlation coefficients (rho) being 0.761 and 0.730 for two input functions. Changing the input function from IDIF to sPBIF had little impact on the correlation patterns between SUV and Patlak parameters.

Objective assessment of lesion detectability of Patlak K_i

Figures 7 and 8 show the TBR and CNR for the mean K_i in lesion VOIs, with corresponding maximum value results provided in Supplemental Figs. 3 and 4. Patlak K_i exhibited higher contrast than SUV in detecting lesions (Fig. 7). However, Patlak K_i did not provide a higher CNR than SUV for detecting malignant lesions (Fig. 8). In benign lesions, K_i had a slightly higher CNR than SUV. The change from IDIF to sPBIF did not affect the detectability of the K_i image.

Correlation between PET parameters and clinicopathological features

The correlation between PET parameters, including SUV and Patlak parameters, and clinicopathological features was also assessed. Most clinicopathological features showed weak correlations with PET parameters, as demonstrated in Fig. 9. However, in Fig. 10, the maximum K_i value in lesion VOIs differentiated between grades of lesion

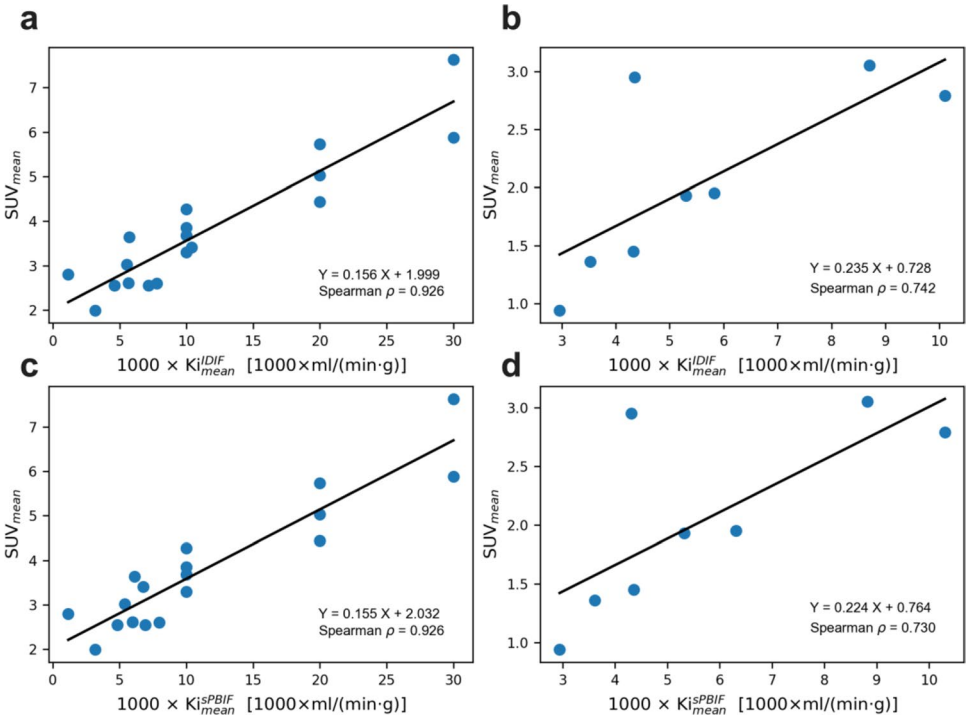

Fig. 5 The correlation between mean value of SUV and Patlak K_i obtained with IDIF or sPBIF in malignant (**a**, **c**) and benign (**b**, **d**) pancreatic lesion VOIs. The correlation between Patlak K_i and SUV is strong in malignant lesions and moderate in benign lesions. The interchange of input functions impacts the correlation insignificantly

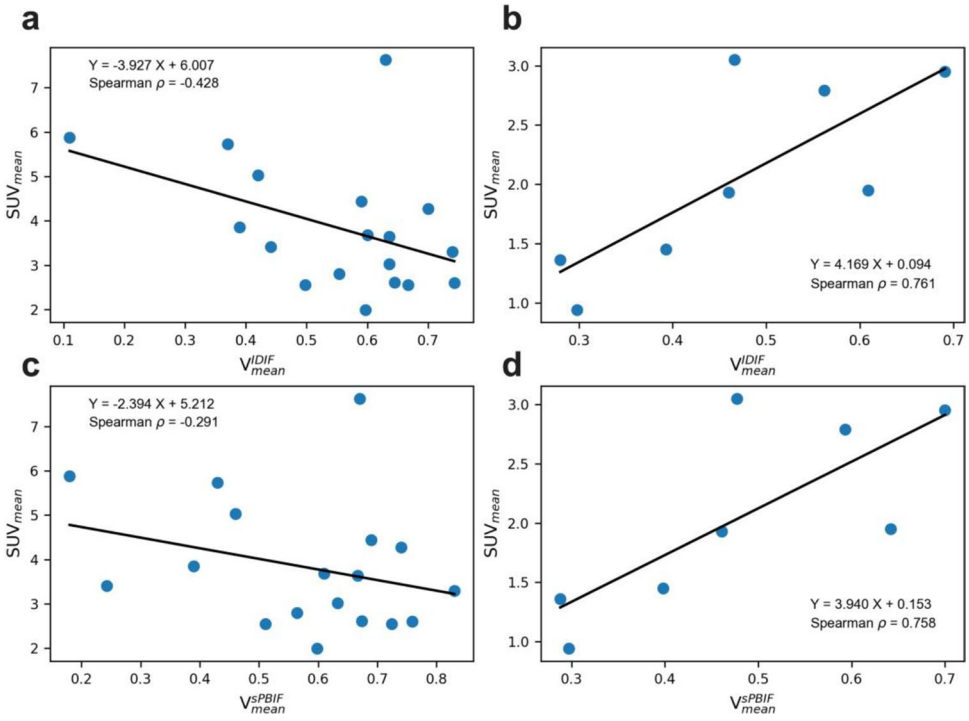

Fig. 6 The correlation between mean value of SUV and Patlak intercept (V_0) obtained with IDIF or sPBIF in malignant (**a**, **c**) and benign (**b**, **d**) pancreatic lesion VOIs. The Patlak V_0 and SUV are weakly correlated in malignant lesions, whereas in benign lesions, they exhibit a positive correlation

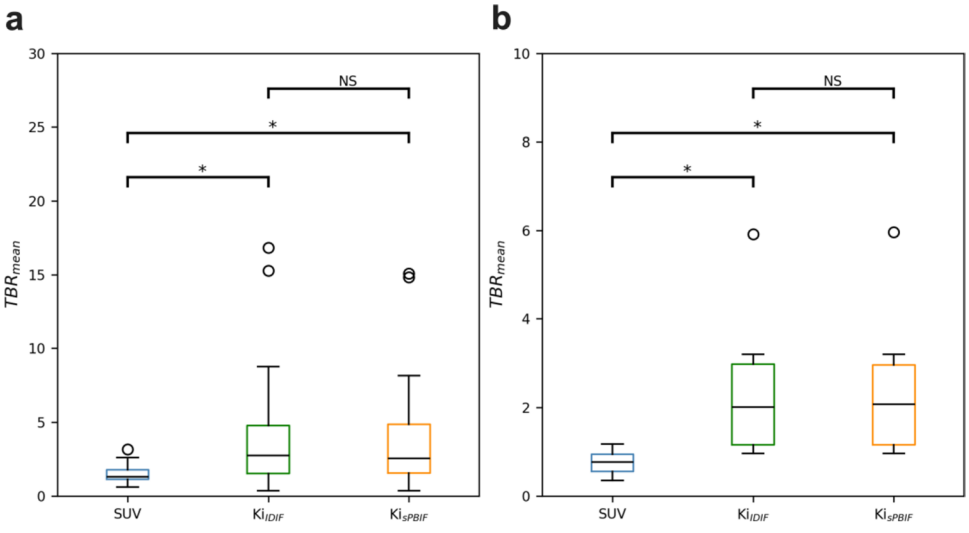

Fig. 7 The comparison of TBRmean (liver as background) among SUV and K_i of two input functions in malignant (**a**) and benign (**b**) pancreatic lesion. The TBRmean of Patlak K_i is significantly higher than that of SUV. The interchange of input function leads to no significant variation of TBRmean

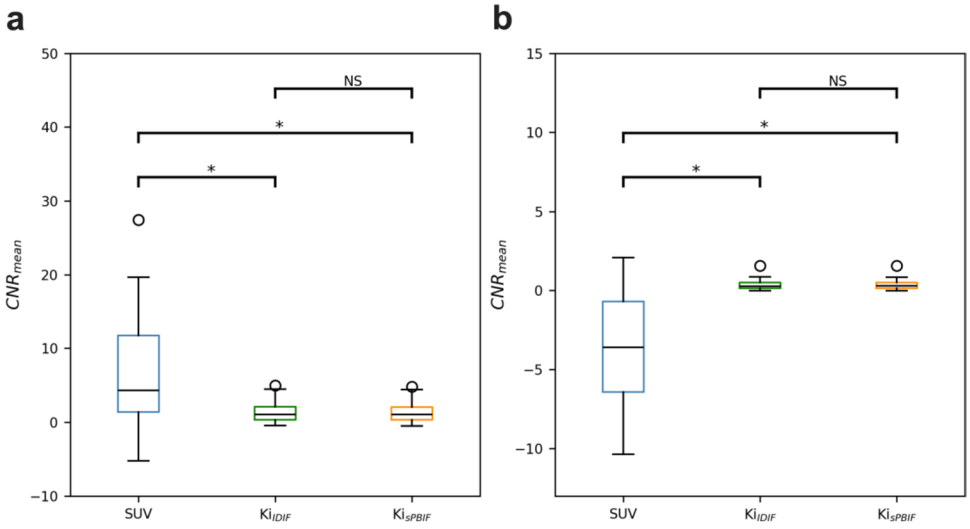

Fig. 8 The comparison of CNRmean (liver as background) among SUV and K_i of two input functions in malignant (**a**) and benign (**b**) pancreatic lesion. The CNRmean of Patlak K_i is significantly lower than that of SUV. The interchange of input function leads to no significant variation of CNRmean

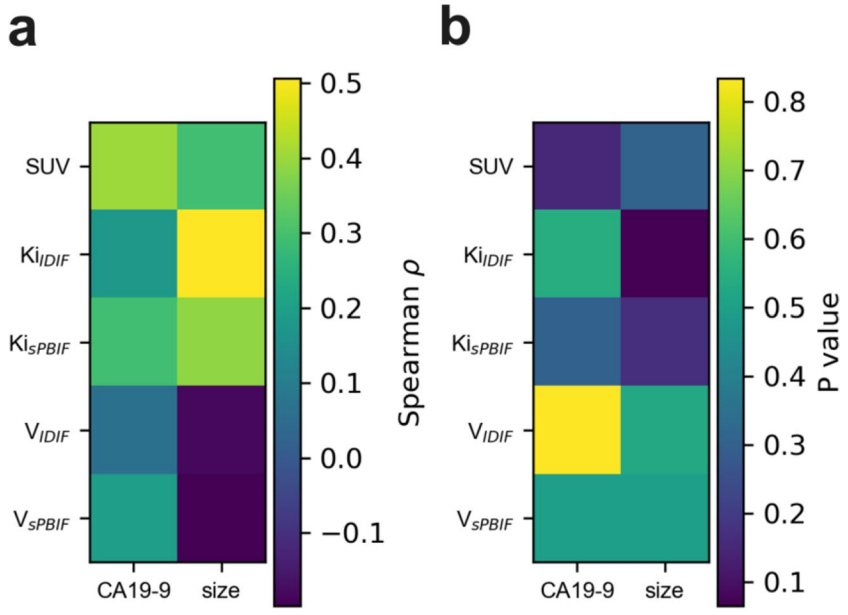

Fig. 9 The correlation coefficients between PET measurements (including SUV and Patlak parameters), CA19-9 and lesion size. CA19-9 and lesion size are weakly correlated with PET measurements. The SUV and Patlak parameters are of the mean value in lesion VOIs

differentiation with a *P*-value of 0.04. The correlation between Patlak parameters and clinicopathological features was minimally affected by changes in the input functions.

Discussion

This study confirms the feasibility of using simplified Patlak parametric imaging with a sPBIF for the 30–50 min post-injection interval in patients with pancreatic cancer. Previous studies have highlighted the convenience of using PBIF to generate Patlak parameters [26, 27, 31, 32]. Our research further examined the clinical value of the simplified

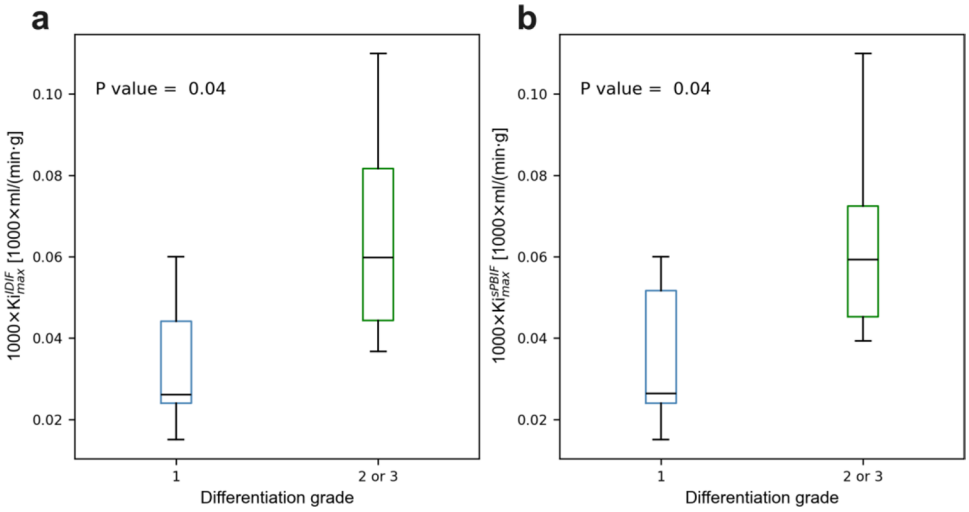

Fig. 10 The comparison of maximum value of K_i obtained with IDIF (**a**) and sPBIF (**b**) between grades of lesion differentiation. The maximum value of Patlak K_i marginally distinguishes the grades of lesion differentiation

sPBIF Patlak parametric imaging in detecting pancreatic lesion. On contrary to IDIF-based parametric imaging where sampling of input function from 0 min after injection is required, only the PET data on the shortened time interval was used with the help of PBIF template. So, the simplified method described in this work made it possible to acquire additional Patlak parametric images along with static SUV imaging. The substitution of IDIF with sPBIF introduced only minimal bias—typically at the percentage or sub-percentage level—into the Patlak parameters within the lesion VOI. The scaling of the PBIF template in uKinetics with activity from a single time point produced biases in the input function AUC and Patlak parameters comparable to those reported in other studies utilizing different scaling methods for PBIF or sPBIF [26, 27, 31, 32]. This excellent consistency in Patlak parameters translated into agreement in subsequent analyses.

The feasibility of simplifying Patlak parametric imaging was assessed in this study by comparing sPBIF with IDIF. Although invasive arterial blood sampling is the gold standard for determining the input function, the feasibility of IDIF for [^{18}F]FDG has been repeatedly demonstrated [17, 19, 20]. The partial volume effect, radiometabolite correction, and BPR are major factors affecting the accuracy of IDIF [22]. The partial volume effect has a negligible impact on IDIF because the PSF technique was included in the PET reconstruction, and a cylindrical VOI with a 4-mm transverse radius on the descending aorta further avoid this effect. The effects of radiometabolite correction and BPR are negligible for [^{18}F]FDG IDIF [17, 19, 20].

The SUV and Patlak parameter values reported in Table 2 are generally consistent with those found in the literature [4]. The higher SUV and K_i values in malignant lesions compared to healthy liver, as shown in Table 2, and the strong correlation between SUV and Patlak K_i in malignant lesions (Pearson ρ = 0.926 for both input functions) in Fig. 5, reflect the characteristic high uptake of [^{18}F]FDG in malignant lesions. Although Patlak K_i in malignant lesions is only marginally higher than in benign lesions, due to its large standard deviation, it suggests that malignant lesions have a greater potential to retain [^{18}F]FDG. The lower Patlak V_0 values in both malignant and benign lesions compared to the liver, as shown in Table 2, indicate that detecting lesions using V_0 images is challenging. In Fig. 6, SUV shows a weak tendency toward a negative correlation

with Patlak V_0 in malignant lesions, whereas in benign lesions, SUV is positively correlated with Patlak V_0. Although this discrepancy seemingly suggests the potential of Patlak V_0 to differentiate between malignant and benign pancreatic lesions, this result does not provide sufficient evidence of its diagnostic potential, as its pharmacokinetic role remains complex and is influenced by various factors [36]. Further investigation is needed to fully understand the value of Patlak parametric imaging in the differential diagnosis of pancreatic cancer.

Patlak K_i parametric imaging provided higher contrast than static imaging for detecting pancreatic lesions. However, the lesion detectability, as measured by CNR on K_i images, was not superior to that of SUV images, likely due to the higher noise levels in Patlak parametric images. Image quality could potentially be improved if parametric images were reconstructed directly from raw data [37], though this approach is less convenient as it requires input function sampling from the time of injection. For the reasons mentioned earlier, detectability was not assessed on Patlak V_0 images.

The maximum K_i value showed some potential for classifying tumor differentiation grades in this study, but its reliability is limited by the noise in K_i images. Previous research has suggested that quantitative [^{18}F]FDG kinetic parameters measured by dynamic PET in newly diagnosed pancreatic cancer correlate with disease aggressiveness, with vascular fraction, K_1, and global influx of [^{18}F]FDG being significant prognostic factors for overall survival in multivariate analysis [38, 39]. [^{18}F]FDG kinetic parameters provide more informative and accurate assessment than visual analysis in primary and recurrent sarcomas, particularly in distinguishing between G I and G III tumors, with a positive predictive value exceeding 80% [40]. For pulmonary lesions, Meng et al. reported that quantitative parameters from fast-kinetics imaging in [^{18}F] FDG PET/CT can differentiate benign from malignant pulmonary lesions and assess Ki-67 expression [41]. Wumener et al. found that K_i demonstrated greater specificity than SUV for the differential diagnosis of lung cancer and could predict epidermal growth factor receptor status with a sensitivity of 0.710 [42]. However, in our study, most clinicopathological features showed weak correlations with PET measurements, possibly due to the small sample size. Further research with larger cohorts is necessary to validate these findings.

This study had several limitations. The small sample size, particularly the limited number of patients with benign pancreatic lesions, was a significant constraint. Additionally, not all pancreatic cancer patients underwent surgery, which limited the availability of complete clinicopathological data. The healthy liver tissue, rather than healthy pancreatic tissue, was used as the only background in the assessment of lesion detectability, due to the difficulty to draw a homogeneous VOI on healthy pancreatic tissue for several subjects. Finally, the PET imaging acquisition time was not optimized for detecting pancreatic lesions.

Conclusions

The use of sPBIF enabled the acquisition of additional Patlak parametric images alongside static SUV imaging in pancreatic cancer patients. Patlak parameters derived from IDIF and sPBIF demonstrated excellent agreement. A strong correlation was observed between SUV and Patlak K_i in pancreatic lesions. Moreover, K_i parametric imaging provided higher contrast than static imaging for the detection of pancreatic lesions.

Abbreviations

AIF	Arterial input function
AUC	Area under curve
BPR	Blood-to-plasma ratio
CA 19 – 9	Carbohydrate antigen 19 – 9
CE-CT	Contrast-enhanced CT
CNR	Contrast-to-noise ratio
FDG	Fluorodeoxyglucose
FOV	Field-of-view
FWHM	Full width at half maximum
IDIF	Image-derived input function
OSEM	Ordered-subset expectation maximization
PBIF	Population-based input function
PDAC	Pancreatic ductal adenocarcinoma
PET	Positron emission tomography
PSF	Point-spread function
SD	Standard deviation
sPBIF	Scaled population-based input function
SUV	Standardized uptake value
TBR	Tumor-to-background ratio
TOF	Time-of-flight
VOI	Volume of interest

Supplementary Information

The online version contains supplementary material available at https://doi.org/10.1186/s40658-025-00758-z.

Supplementary Material

Acknowledgements
Not applicable.

Author contributions
All authors contributed to the study's conception and design. Material preparation and data collection were carried out by ZH (Zhixin Hao), HZ, YD, JQ, XY, ZH (Zhenghai Huang), and CR. Data analysis was performed by ZH (Zhixin Hao), HZ, and MY. ZH (Zhixin Hao) and HZ wrote the first draft of the manuscript. All authors provided feedback on earlier versions of the manuscript and read and approved the final version.

Funding
This work was supported by the National Natural Science Foundation of China (Grant No. 82071967); Chinese Academy of Medical Sciences (CAMS) Innovation Fund for Medical Sciences (CIFMS) (Grant No. CIFMS-2023-I2M-2-002, CIFMS-2021-I2M-1-002, CIFMS-2021-I2M-1-003, CIFMS-2021-I2M-1-025); and the National High Level Hospital Clinical Research Funding (Grant No. 2022-PUMCH-D-001, 2022-PUMCH-D-002).

Data availability
The datasets used and analysed during the current study are available from the corresponding author on reasonable request.

Declarations

Ethics approval and consent to participate
This study was performed in line with the principles of the Declaration of Helsinki. Ethical approval was obtained from the Institutional Review Board of Peking Union Medical University Hospital (Approval No. K4068). Informed consent was obtained from all individual participants included in the study.

Consent for publication
Not applicable.

Competing interests
The authors declare that they have no competing interests.

Received: 17 September 2024 / Accepted: 30 April 2025
Published online: 20 May 2025

References

1. Rahib L, Smith BD, Aizenberg R, Rosenzweig AB, Fleshman JM, Matrisian LM. Projecting cancer incidence and deaths to 2030: the unexpected burden of thyroid, liver, and pancreas cancers in the united States. Cancer Res. 2014;74:2913–21. https://doi.org/10.1158/0008-5472.CAN-14-0155.
2. Lee ES, Lee JM. Imaging diagnosis of pancreatic cancer: a state-of-the-art review. World J Gastroenterol. 2014;20:7864–77. https://doi.org/10.3748/wjg.v20.i24.7864.

3. Schwenck J, Sonanini D, Cotton JM, Rammensee HG, la Fougere C, Zender L, et al. Advances in PET imaging of cancer. Nat Rev Cancer. 2023;23:474–90. https://doi.org/10.1038/s41568-023-00576-4.
4. Dias AH, Hansen AK, Munk OL, Gormsen LC. Normal values for (18)F-FDG uptake in organs and tissues measured by dynamic whole body multiparametric FDG PET in 126 patients. EJNMMI Res. 2022;12:15. https://doi.org/10.1186/s13550-022-00884-0.
5. Zhang X, Cherry SR, Xie Z, Shi H, Badawi RD, Qi J. Subsecond total-body imaging using ultrasensitive positron emission tomography. Proc Natl Acad Sci U S A. 2020;117:2265–7. https://doi.org/10.1073/pnas.1917379117.
6. Viswanath V, Chitalia R, Pantel AR, Karp JS, Mankoff DA. Analysis of Four-Dimensional data for total body PET imaging. PET Clin. 2021;16:55–64. https://doi.org/10.1016/j.cpet.2020.09.009.
7. Sperti C, Pasquali C, Decet G, Chierichetti F, Liessi G, Pedrazzoli S. F-18-fluorodeoxyglucose positron emission tomography in differentiating malignant from benign pancreatic cysts: a prospective study. J Gastrointest Surg. 2005;9. https://doi.org/10.1016/j.gassur.2004.10.002. 22– 8; discussion 8–9.
8. Saif MW, Cornfeld D, Modarresifar H, Ojha B. 18F-FDG positron emission tomography CT (FDG PET-CT) in the management of pancreatic cancer: initial experience in 12 patients. J Gastrointestin Liver Dis. 2008;17:173–8.
9. Daamen LA, Groot VP, Goense L, Wessels FJ, Borel Rinkes IH, Intven MPW, et al. The diagnostic performance of CT versus FDG PET-CT for the detection of recurrent pancreatic cancer: a systematic review and meta-analysis. Eur J Radiol. 2018;106:128–36. https://doi.org/10.1016/j.ejrad.2018.07.010.
10. Zhang J, Jia G, Zuo C, Jia N, Wang H. (18)F- FDG PET/CT helps differentiate autoimmune pancreatitis from pancreatic cancer. BMC Cancer. 2017;17:695. https://doi.org/10.1186/s12885-017-3665-y.
11. Pakzad F, Groves AM, Ell PJ. The role of positron emission tomography in the management of pancreatic cancer. Semin Nucl Med. 2006;36:248–56. https://doi.org/10.1053/j.semnuclmed.2006.03.005.
12. Jha P, Bijan B. PET/CT for pancreatic malignancy: potential and pitfalls. J Nucl Med Technol. 2015;43:92–7. https://doi.org/10.2967/jnmt.114.145458.
13. Patlak CS, Blasberg RG, Fenstermacher JD. Graphical evaluation of blood-to-brain transfer constants from multiple-time uptake data. J Cereb Blood Flow Metab. 1983;3:1–7. https://doi.org/10.1038/jcbfm.1983.1.
14. Patlak CS, Blasberg RG. Graphical evaluation of blood-to-brain transfer constants from multiple-time uptake data. Generalizations J Cereb Blood Flow Metab. 1985;5:584–90. https://doi.org/10.1038/jcbfm.1985.87.
15. Logan J, Fowler JS, Volkow ND, Wolf AP, Dewey SL, Schlyer DJ, et al. Graphical analysis of reversible radioligand binding from time-activity measurements applied to [N-11 C-methyl]-(-)-cocaine PET studies in human subjects. J Cereb Blood Flow Metab. 1990;10:740–7. https://doi.org/10.1038/jcbfm.1990.127.
16. Lammertsma AA, Bench CJ, Hume SP, Osman S, Gunn K, Brooks DJ, et al. Comparison of methods for analysis of clinical [11 C]raclopride studies. J Cereb Blood Flow Metab. 1996;16:42–52. https://doi.org/10.1097/00004647-199601000-00005.
17. Gambhir SS, Schwaiger M, Huang SC, Krivokapich J, Schelbert HR, Nienaber CA, et al. Simple noninvasive quantification method for measuring myocardial glucose utilization in humans employing positron emission tomography and fluorine-18 Deoxyglucose. J Nucl Med. 1989;30:359–66.
18. Ohtake T, Kosaka N, Watanabe T, Yokoyama I, Moritan T, Masuo M, et al. Noninvasive method to obtain input function for measuring tissue glucose utilization of thoracic and abdominal organs. J Nucl Med. 1991;32:1432–8.
19. Palard-Novello X, Visser D, Tolboom N, Smith CLC, Zwezerijnen G, van de Giessen E, et al. Validation of image-derived input function using a long axial field of view PET/CT scanner for two different tracers. EJNMMI Phys. 2024;11:25. https://doi.org/10.1186/s40658-024-00628-0.
20. de Geus-Oei LF, Visser EP, Krabbe PF, van Hoorn BA, Koenders EB, Willemsen AT, et al. Comparison of image-derived and arterial input functions for estimating the rate of glucose metabolism in therapy-monitoring 18F-FDG PET studies. J Nucl Med. 2006;47:945–9.
21. Zanotti-Fregonara P, Fadaili el M, Maroy R, Comtat C, Souloumiac A, Jan S, et al. Comparison of eight methods for the Estimation of the image-derived input function in dynamic [(18)F]-FDG PET human brain studies. J Cereb Blood Flow Metab. 2009;29:1825–35. https://doi.org/10.1038/jcbfm.2009.93.
22. Zanotti-Fregonara P, Chen K, Liow JS, Fujita M, Innis RB. Image-derived input function for brain PET studies: many challenges and few opportunities. J Cereb Blood Flow Metab. 2011;31:1986–98. https://doi.org/10.1038/jcbfm.2011.107.
23. Rissanen E, Tuisku J, Luoto P, Arponen E, Johansson J, Oikonen V, et al. Automated reference region extraction and population-based input function for brain [(11)C]TMSX PET image analyses. J Cereb Blood Flow Metab. 2015;35:157–65. https://doi.org/10.1038/jcbfm.2014.194.
24. Contractor KB, Kenny LM, Coombes CR, Turkheimer FE, Aboagye EO, Rosso L. Evaluation of limited blood sampling population input approaches for kinetic quantification of [18F]fluorothymidine PET data. EJNMMI Res. 2012;2:11. https://doi.org/10.1186/2191-219X-2-11.
25. Zanotti-Fregonara P, Hirvonen J, Lyoo CH, Zoghbi SS, Rallis-Frutos D, Huestis MA, et al. Population-based input function modeling for [(18)F]FMPEP-d 2, an inverse agonist radioligand for cannabinoid CB1 receptors: validation in clinical studies. PLoS ONE. 2013;8:e60231. https://doi.org/10.1371/journal.pone.0060231.
26. Sari H, Eriksson L, Mingels C, Alberts I, Casey ME, Afshar-Oromieh A, et al. Feasibility of using abbreviated scan protocols with population-based input functions for accurate kinetic modeling of [(18)F]-FDG datasets from a long axial FOV PET scanner. Eur J Nucl Med Mol Imaging. 2023;50:257–65. https://doi.org/10.1007/s00259-022-05983-7.
27. van Sluis J, Yaqub M, Brouwers AH, Dierckx R, Noordzij W, Boellaard R. Use of population input functions for reduced scan duration whole-body Patlak (18)F-FDG PET imaging. EJNMMI Phys. 2021;8:11. https://doi.org/10.1186/s40658-021-00357-8.
28. Fahrni G, Karakatsanis NA, Di Domenicantonio G, Garibotto V, Zaidi H. Does whole-body Patlak (18)F-FDG PET imaging improve lesion detectability in clinical oncology? Eur Radiol. 2019;29:4812–21. https://doi.org/10.1007/s00330-018-5966-1.
29. Zaker N, Kotasidis F, Garibotto V, Zaidi H. Assessment of lesion detectability in dynamic Whole-Body PET imaging using compartmental and Patlak parametric mapping. Clin Nucl Med. 2020;45:e221–31. https://doi.org/10.1097/RLU.0000000000002954.
30. Dias AH, Pedersen MF, Danielsen H, Munk OL, Gormsen LC. Clinical feasibility and impact of fully automated multiparametric PET imaging using direct Patlak reconstruction: evaluation of 103 dynamic whole-body (18)F-FDG PET/CT scans. Eur J Nucl Med Mol Imaging. 2021;48:837–50. https://doi.org/10.1007/s00259-020-05007-2.

31. Dias AH, Smith AM, Shah V, Pigg D, Gormsen LC, Munk OL. Clinical validation of a population-based input function for 20-min dynamic whole-body (18)F-FDG multiparametric PET imaging. EJNMMI Phys. 2022;9:60. https://doi.org/10.1186/s40658-022-00490-y.
32. Pavoine M, Thuillier P, Karakatsanis N, Legoupil D, Amrane K, Floch R, et al. Clinical application of a population-based input function (PBIF) for a shortened dynamic whole-body FDG-PET/CT protocol in patients with metastatic melanoma treated by immunotherapy. EJNMMI Phys. 2023;10:79. https://doi.org/10.1186/s40658-023-00601-3.
33. Li G, Ma W, Li X, Yang W, Quan Z, Ma T, et al. Performance evaluation of the uMI panorama PET/CT system in accordance with the National electrical manufacturers association NU 2-2018 standard. J Nucl Med. 2024. https://doi.org/10.2967/jnumed.123.265929.
34. Wu Q, Gu F, Gu Y, Liu Y, Shi F, Xu T, et al. Impact of equilibration time (t*) on Patlak quantitation in dynamic total-body imaging using the uEXPLORER PET scanner. Soc Nuclear Med; 2022.
35. Ye Q, Zeng H, Zhao Y, Zhang W, Dong Y, Fan W, et al. Framing protocol optimization in oncological Patlak parametric imaging with uKinetics. EJNMMI Phys. 2023;10:54. https://doi.org/10.1186/s40658-023-00577-0.
36. Laffon E, Marthan R. Is Patlak y-intercept a relevant metrics? Eur J Nucl Med Mol Imaging. 2021;48:1287–90. https://doi.org/10.1007/s00259-020-04954-0.
37. Wang G, Qi J. Acceleration of the direct reconstruction of linear parametric images using nested algorithms. Phys Med Biol. 2010;55:1505–17. https://doi.org/10.1088/0031-9155/55/5/016.
38. Epelbaum R, Frenkel A, Haddad R, Sikorski N, Strauss LG, Israel O, et al. Tumor aggressiveness and patient outcome in cancer of the pancreas assessed by dynamic 18F-FDG PET/CT. J Nucl Med. 2013;54:12–8. https://doi.org/10.2967/jnumed.112.107466.
39. Salavati A, Saboury B, Alavi A. Comment on: tumor aggressiveness and patient outcome in cancer of the pancreas assessed by dynamic 18F-FDG PET/CT. J Nucl Med. 2014;55:350–1. https://doi.org/10.2967/jnumed.113.130138.
40. Dimitrakopoulou-Strauss A, Strauss LG, Schwarzbach M, Burger C, Heichel T, Willeke F, et al. Dynamic PET 18F-FDG studies in patients with primary and recurrent soft-tissue sarcomas: impact on diagnosis and correlation with grading. J Nucl Med. 2001;42:713–20.
41. Meng N, Zhang M, Ren J, Fu F, Xie B, Wu Y, et al. Quantitative parameters of static imaging and fast kinetics imaging in (18)F-FDG total-body PET/CT for the assessment of histological feature of pulmonary lesions. Quant Imaging Med Surg. 2023;13:5579–92. https://doi.org/10.21037/qims-23-186.
42. Wumener X, Zhang Y, Zang Z, Du F, Ye X, Zhang M, et al. The value of dynamic FDG PET/CT in the differential diagnosis of lung cancer and predicting EGFR mutations. BMC Pulm Med. 2024;24:227. https://doi.org/10.1186/s12890-024-02997-9.

Publisher's note